RESEARCH ARTICLE

WILEY

Assessing the coupling between local neural activity and global connectivity fluctuations: Application to human intracranial electroencephalography during a cognitive task

Manel Vila-Vidal[1,2] 🆔 | **Mariam Khawaja**[3] | **Mar Carreño**[3,4] | **Pedro Roldán**[5] |
Jordi Rumià[5] | **Antonio Donaire**[3,4,6] | **Gustavo Deco**[2,7] | **Adrià Tauste Campo**[1,2] 🆔

[1]Center for Brain and Cognition, Department of Information and Communication Technologies, Universitat Pompeu Fabra, Barcelona, Spain

[2]Computational Biology and Complex Systems Group, Department of Physics, Universitat Politècnica de Catalunya, Barcelona, Spain

[3]Epilepsy Program, Hospital Clínic, Barcelona, Spain

[4]Institut d'Investigacions Biomèdiques August Pi i Sunyer (IDIBAPS), Barcelona, Spain

[5]Epilepsy Program, Neurosurgery, Hospital Clínic, Barcelona, Spain

[6]CIBERBBN, Networking Centre on Bioengineering, Biomaterials and Nanomedicine, Barcelona, Spain

[7]Institució Catalana de Recerca i Estudis Avançats, Barcelona, Spain

Correspondence
Manel Vila-Vidal, Universitat Pompeu Fabra, Edifici Merce Rodereda, C. de Ramon Trias Fargas, 25, 08005 Barcelona, Spain.
Email: m@vila-vidal.com

Adrià Tauste Campo, Universitat Politècnica de Catalunya, Escola Politècnica Superior d'Edificació de Barcelona, Av. Dr. Marañon 44-50, 08028 Barcelona, Spain.
Email: adria.tauste@upc.edu

Abstract

Cognitive-relevant information is processed by different brain areas that cooperate to eventually produce a response. The relationship between local activity and global brain states during such processes, however, remains for the most part unexplored. To address this question, we designed a simple face-recognition task performed in patients with drug-resistant epilepsy and monitored with intracranial electroencephalography (EEG). Based on our observations, we developed a novel analytical framework (named "local–global" framework) to statistically correlate the brain activity in every recorded gray-matter region with the widespread connectivity fluctuations as proxy to identify concurrent local activations and global brain phenomena that may plausibly reflect a common functional network during cognition. The application of the local–global framework to the data from three subjects showed that similar connectivity fluctuations found across patients were mainly coupled to the local activity of brain areas involved in face information processing. In particular, our findings provide preliminary evidence that the reported global measures might be a novel signature of functional brain activity reorganization when a stimulus is processed in a task context regardless of the specific recorded areas.

KEYWORDS
cognitive task, intracranial EEG, spectral estimation, local activity, global connectivity

Gustavo Deco and Adrià Tauste Campo jointly supervised this work.

1 | INTRODUCTION

Human cognition implies the contribution of different brain areas that interact to process incoming information and eventually produce a response. A classical localist approach in cognitive neuroscience has attempted to assign cognitive functions to specific brain areas and understand their role at different stages of the cognitive process. This approach has proven successful in partially explaining a number of cognitive processes such as attention, memory, or decision making with different recording modalities (Brunel & Wang, 2001; Deco & Rolls, 2005; Hubel & Wiesel, 1959; Kahana, 2006; Lachaux et al., 2012; Wang, 2002). In sharp contrast, more recent studies have taken a globalist approach, focusing on brain states that can be measured by means of statistical dependencies across the whole brain (Axmacher et al., 2008; Bassett et al., 2011; Bressler & Menon, 2010; Cruzat et al., 2018; Deco et al., 2015; Palva et al., 2010; Sporns et al., 2005; Wang et al., 2015). Yet, a fundamental question linking the two perspectives remains for the most part unaddressed: how does the processing of cognitive-relevant information in each functionally involved brain area relate to the brain's global state?

To tackle this question, we designed a simple face-recognition paradigm that patients with drug-resistant epilepsy conducted during the presurgical intracranial monitoring period (Engel et al., 2005; Kahane et al., 2003; Lachaux et al., 2003; Munari & Bancaud, 1985). During this procedure, the intracranial activity of up to 200 electrode contacts in varied regions from cortical and subcortical areas is simultaneously recorded, which sheds light into the mechanisms of neural activity associated with consciously perceiving and reporting a visual stimulus. In particular, we collected intracranial electroencephalography (iEEG) data (also often referred in the literature as local field potentials, LFP) from depth electrodes stereotactically implanted stereoelectroencephalography (SEEG) for presurgical diagnosis in three drug-resistant epilepsy patients while they were performing the cognitive task.

Inspired by the recorded data, we developed and systematized a methodological pipeline integrating neuroanatomic information, clinical reports, signal processing functions and statistical analysis, with the aim to localize and quantify time-varying human neural activity in the context of a cognitive task. High-frequency LFP power is known to display high correlation with spiking activity of local neuronal assemblies (Hipp et al., 2012; Pesaran et al., 2018). Based on these results, we used LFP high-frequency power activations as proxy for locally generated activity. Yet, the specific frequency range of such activity can vary depending on the type of LFP recording technique. To avoid making further assumptions, we adopted a data-driven approach and defined the frequency range depending on the observed activations. In order to characterize global network states, we resorted to functional connectivity analysis. Activity in the beta band and below is known to display long-range coherence and it is thought to have a more widespread origin (Pesaran et al., 2018), reflecting possible concurrent inputs or more

global states. Based on these premises, we defined two independent functions in the low-frequency range to measure the brain sites' connectivity consistency across time and across trials. In addition, we took advantage of the referential montage to capture these global cofluctuations, as suggested by previous literature (Tauste Campo et al., 2018). As a result of our work, we propose a novel data-analysis framework (named "local–global" framework) that statistically correlates across time the brain activity in every gray-matter recording site with the predefined connectivity functions to assess the coupling between local neural activations and the brain's global connectivity during cognition. We first applied this framework to the data gathered from two patients with epilepsy conducting the same task paradigm, showing that global connectivity fluctuations were temporally associated with variations of local activity in task-relevant areas. Finally, we validated our methodology in a third subject with a slightly different task paradigm confirming most of our previous findings.

2 | METHODS

2.1 | Ethics statement

The study was conducted in accordance with the Declaration of Helsinki and informed consent was explicitly obtained from all participants prior to the recordings and the performance of the tasks. All diagnostic, surgical and experimental procedures have been previously approved by The Clinical Ethical Committee of Hospital Clínic (Barcelona, Spain). In particular, the specific proposal to run the cognitive experiments for this study was approved in March 2020 under the code number HCB/2020/0182.

2.2 | Participants and behavioral task

Intraranial EEG recordings during performance of certain tasks were acquired in two subjects with pharmacoresistant epilepsy during the diagnostic monitoring period in Hospital Clínic (Barcelona, Spain). Details on patients' demographic information are given in Table 1. The two participants had normal or corrected-to-normal vision. The task was designed to characterize brain responses to static face recognition. Stimulus presentation was designed and responses were collected using Psychtoolbox 3 for Matlab.

Subjects viewed N (64 and 71 for subjects 1 and 2, respectively) face images of different identities on a laptop screen. Approximately one half of these images were familiar faces and the remaining half were images from people that the subject was unlikely to know. Familiar faces were selected after a short interview with the subject in which they introduced themselves and talked about their hobbies and interests. Potentially unfamiliar faces were extracted from an

TABLE 1 Demographic data

Subject	Sex	Age (years)	Epilepsy onset (years)	Suspected epileptic focus	Hand laterality	Implantation	Number of electrodes (right/left)	Number of contacts (right/left)	Number of contacts included in analysis
1	F	51	27	Right lateral frontal/insula (FCD)	Right	Right	16/0	175/0	47
2	M	49	15	Left dorso-medial frontal	Right	Left	0/7	0/93	26

Abbreviations: F, female; FCD, focal cortical dysplasia; M, male.

extensive database and were selected according to the age, country and background of the subject. Face images had a resolution of 160×160 pixels, and were presented at the center of the screen framed by thin lines that randomly changed their color (green and red) from image to image presentation to help the subject maintain attention. Each trial (Figure 1a) started with a prestimulus blank screen that lasted $ITI = 0.5$ ms (intertrial interval), then a face image was presented during time T_{stim} (1 and 0.9 s for subjects 1 and 2, respectively). Subjects were instructed to pay attention to the presented face image and then, after the face went off the screen, to respond during a maximum timeout of T_{out} (10 and 3 s for subjects 1 and 2, respectively) whether they recognized the specific person by pressing the trigger button of a joystick with the right hand. Either after pressing the joystick or when the maximum response timeout had elapsed, the next trial started as stated above. The parameters were adjusted depending on cognitive and experimental constraints associated with each subject. This task lasted in total between 5 and 12 min. Subject 1 experienced psychotic symptoms later on during the day of the task. We therefore decided to disregard all behavioral responses (recognized vs. nonrecognized) from our analysis in this subject.

Across our initial study (subjects 1 and 2), we analyzed the data in two different settings: a stimulus-presentation-locked setting (subjects 1 and 2) and a motor-locked setting (subject 2). To further validate our methodology, we independently analyzed data from another subject (subject 3) that performed a cognitive task under a slightly different paradigm. Details about this patient can be found in Table S1. The task consisted of a total of 96 trials, with a similar structure to those of the main paradigm, which allowed for both stimulus and motor-locked analyses. In this case, however, each trial was preceded by a fixation cross that lasted 0.5 ms and that was meant to reset the subject's attention. Although this difference might affect the cognitive processes involved in the task, the aim of this secondary analysis was to cross-validate some of our method's assumptions and findings with a different dataset.

2.3 | Data acquisition

LFPs were recorded using 16, 7 and 13 (subjects 1-3, respectively) intracerebral multiple contact Microdeep® platinum–iridium Depth

Electrodes (Dixi Medical, Besançon, France; diameter: 0.8 mm; 5–18 contacts, contact length: 2 mm, distance between contacts: 1.5 mm) that were stereotactically implanted using frameless stereotaxy, neuronavigation assisted, and intraoperative CT-guided O-Arm and the Vertek articulated passive arm. In total, 175, 93, and 147 contacts were implanted and recorded in subjects 1–3, respectively (see Tables 1 and S2 for details and Figure 1b for an example of the implantation scheme of subject 1). The decision to implant, the selection of the electrode targets and the implantation duration were entirely made on clinical grounds using the standard procedure (Cardinale et al., 2013; Lachaux et al., 2003). All recordings were obtained using a standard clinical EEG system (XLTEK, subsidiary of Natus Medical) with a 2048 Hz sampling rate. All signals were referenced to the scalp electrode CPz.

Individual pre- and postimplant T1-weighted magnetic resonance (MR) scans were used to determine contact localizations. MR scans were obtained with a 1.5 T unit (Magnetom Aera 1.5 T; Siemens Medical Systems, Erlangen, Germany) with a specific protocol that included the following sequence: sagittal T1-weighted gradient recalled (repetition time [TR] 20 ms, echo time [TE] 7.38 ms, Flip Angle [FA] 20°, 1 mm slice thickness).

2.4 | Anatomical localization of the SEEG electrode contacts and definition of regions of interest

Contact anatomical locations were directly identified from the individual subjects' postimplant MRI (magnetic resonance imaging) by visual inspection (MVV), where contacts can be distinguished as dark spherical artifacts (diameter ≈ 3 mm; see Figure 1b). MRI images were analyzed using the DICOM Viewer Osirix Lite (v.12.0.1). Contact localization within brain structures were therefore obtained with an error of the contact midpoint of approximately 1.5 mm. First, contacts were labeled either as gray matter (GM) or white matter (WM). Previous research suggests that electrical fields generated in GM can be measured by contacts in nearby WM up to ≈ 1 mm away (Arnulfo et al., 2015; Buzsáki et al., 2012; Narizzano et al., 2017). Based on this assumption, WM contacts lying at a distance below 1 mm from GM regions with no contact inside were assigned to that region and classified as GM. Contacts lying outside brain tissue or within altered brain
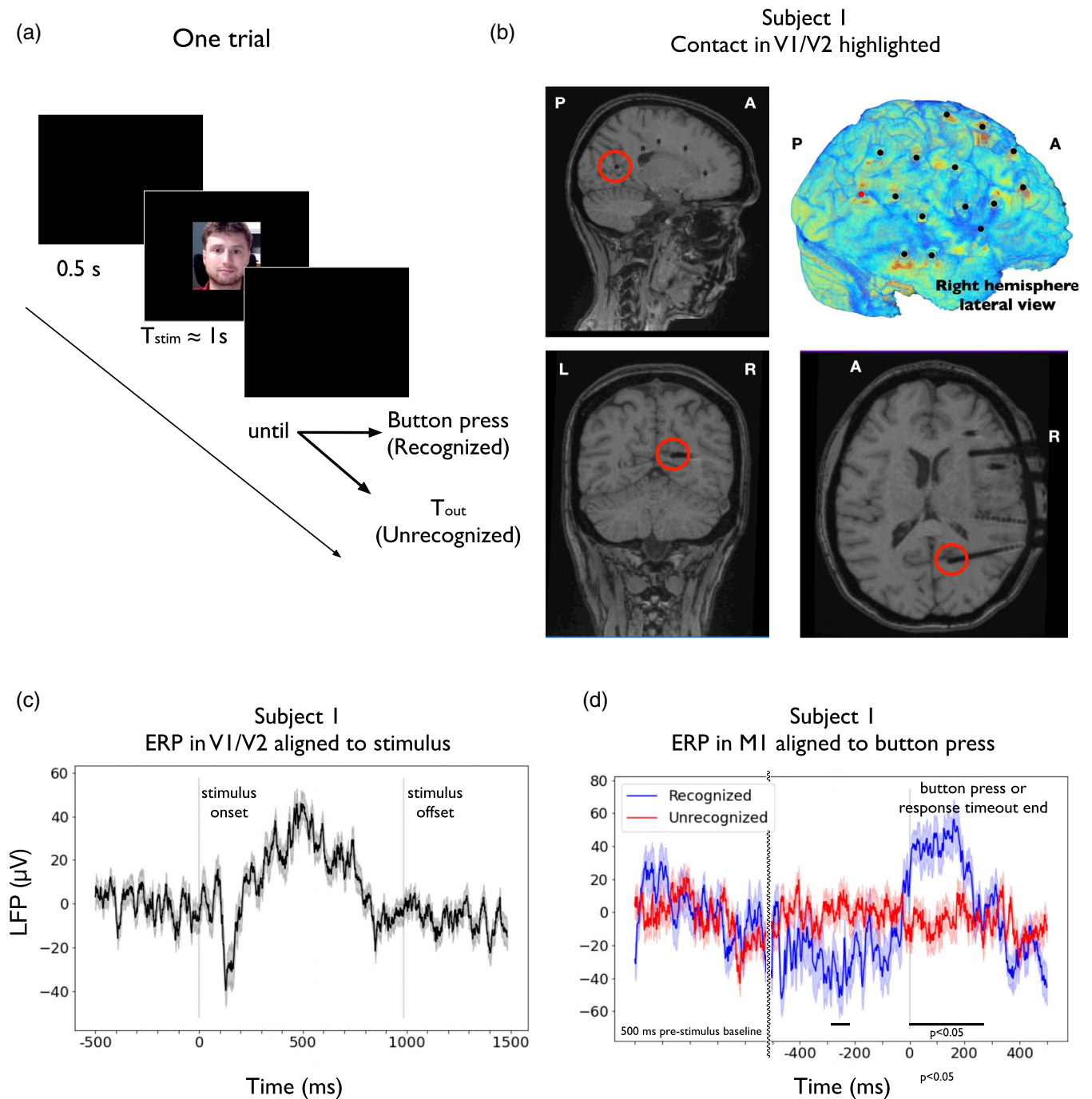
(a) **One trial**

0.5 s

$T_{stim} \approx 1s$

until → Button press (Recognized)

T_{out} (Unrecognized)

(b) **Subject 1**
Contact in V1/V2 highlighted

Right hemisphere lateral view

(c) **Subject 1**
ERP in V1/V2 aligned to stimulus

(d) **Subject 1**
ERP in M1 aligned to button press

FIGURE 1 Experimental protocol, recording locations and neural responses. (a) Schematic representation of the behavioral task. Each trial consists of a prestimulus blank screen lasting 0.5 ms, a face image that remains present for approximately 1 s and a blank screen, where the subject has to report whether they recognized the person by pressing a trigger button. Alternatively, the trial ends after a maximum response timeout T_{out}. (b) Subject 1 postimplantation MRI brain scans showing different electrode trajectories in sagittal, coronal and horizontal planes (from top left to bottom right) and 3D brain reconstruction (top right). The red circles highlight the trajectory of the electrode pointing towards the primary and secondary visual areas. (c) Event-related potential (ERP) in V1/V2 (deepest electrode contact of the trajectory highlighted in (b)) aligned to stimulus presentation (median ± SEM across $N = 64$ trials). Signals were baseline-corrected on a trial-by-trial basis (baseline from 500 to 0 ms before stimulus presentation) before averaging. Vertical dark lines indicate the stimulus onset and offset times, respectively. (d) Event-related potential (ERP) in M1 (right-hand region) during recognized (button press with left hand, blue, median ± SEM across $N = 21$ trials) and nonrecognized (timeout end, red, median ± SEM across $N = 49$ trials) trials aligned to button press or response timeout end, respectively (vertical dark line). Signals were baseline-corrected on a trial-by-trial basis (baseline from 500 to 0 ms before stimulus presentation) before averaging. Prestimulus baseline is also shown for comparison. Curvy line marks time discontinuity. In this case, we tested differences in the signals between both conditions. Black bars indicate time periods with significant differences between conditions (Ranksum test at each time point and across conditions, with a criterion of $p < .05$ for a minimum of 102 consecutive samples, 50 ms)

TABLE 2 Implantation scheme

ROI	P1		P2	
	#Electrodes	#Contacts	#Electrodes	#Contacts
Rostral anterior cingulate	1	1	2	3
Caudal anterior cingulate	1	2	1	1
Posterior cingulate	1	2	1	2
Isthmus cingulate	1	2	1	1
Insula	0	0	1	1
Cuneus	1	3	0	0
Supramarginal	2	7	0	0
Inferior temporal	1	1	0	0
Middle temporal	2	6	0	0
Superior temporal	2	8	2	6
Superior frontal	0	0	1	1
Precentral	1	3	1	3
Pars triangularis	0	0	1	3
Caudal middle frontal	1	3	0	0
Rostral middle frontal	2	5	2	5
Hippocampus	2	4	0	0
Total	18	47	13	26

Note: Regions of interest monitored in each patient are expressed in terms of the Desikan–Killiany atlas with an extra ROI for the hippocampus.

tissue according to clinicians (e.g., heterotopias, focal cortical dysplasias) were excluded from the analysis. The electrode contacts lying in the suspected epileptic focus were identified by clinical experts using gold-standard procedures and were also excluded from the study.

GM contact locations were expressed in terms of the Desikan–Killiany (Desikan et al., 2006) brain atlas (34 region of interests (ROI) per hemisphere), with an extra ROI for the hippocampus, by visually identifying well-defined anatomical landmarks (MVV). Table 2 summarizes the number of contacts and electrodes in each ROI for both subjects. See Table S2 for details about the third subject. Contacts were also approximately mapped to Brodmann areas, when possible. For further validation, automatic parcellations were created using the postimplant MRI scans and the Free-surfer software, which confirmed manual localizations. GM contacts were also mapped, when possible, to functional ROIs (regions of interest) as usually expressed in the cognitive literature based on fMRI and electrophysiological studies (e.g., V1/V2, DLPFC, VLPFC, M1, PMC), which were also confirmed by a neurologist (MK).

For the purpose of this study, V1/V2 was defined roughly as the primary and/or secondary visual cortices. The DLPFC (dorsolateral prefrontal cortex) was defined roughly as the middle frontal gyrus, the VLPFC (ventro-lateral prefrontal cortex) was defined as the inferior frontal gyrus and the superior parts of the pars triangularis, pars orbitalis and pars opercularis. M1 (primary motor cortex) was defined as the precentral gyrus and PMC (premotor cortex) was roughly defined as corresponding to Brodmann area 6, that is, as a vertical strip extending from the cingulate sulcus to the lateral sulcus, including caudal portions of the superior frontal and middle frontal gyri, and

rostrally bounded by the precentral gyrus. The remaining ROIs were referred to using its denomination in the Desikan–Killiany atlas. In particular, for this study: supramarginal gyrus (SMG), insula (I), inferior temporal gyrus (ITG), middle temporal gyrus (MTG), superior temporal gyrus (STG), ventral anterior cingulate cortex (vACC), dorsal anterior cingulate cortex (dACC), and a single posterior cingulate cortex (PCC), under which we grouped the posterior cingulate and the isthmus cingulate.

2.5 | Signal preprocessing

Besides the contacts mentioned in Section 2.4, we also excluded from the computational analysis contacts displaying highly nonphysiological activity. SEEG signals were preprocessed and analyzed using custom-made code in Python 3 based on the Numpy, Scipy, and MNE libraries. Signals were analyzed in the monopolar montage (reference to CPz). The choice to use monopolar montage was based both on theoretical and practical considerations. Bipolar referencing is commonly used in LFP analyses to remove volume conducted components and isolate local activity originated in the vicinity of each contact. This can be achieved thanks to a very high spatial resolution, with a spacing between contacts around 0.1 mm. With standard SEEG electrodes, however, the distance between contacts is typically much larger and in certain settings bipolar montage might introduce distantly generated components and remove common activity not caused by volume conduction (see Zaveri et al., 2006 for a discussion of potential alterations introduced by bipolar montage in intracranial EEG). In addition,

our previous experience also suggests that monopolar might better capture local activity (Vila-Vidal et al., 2020) and global connectivity states (Tauste Campo et al., 2018) with SEEG. However, volume conduction to neighboring contacts cannot be excluded from monopolar montage either. This was taken into account and corrected for when computing global variables, as will be later described. To validate our choice, we also repeated the analyses using the bipolar and the closest-white-matter montages in one patient and compared the results (see Supplementary Information, and Figures S10 and S11).

Prior to the main analysis, signals were low-pass filtered with a zero-phase FIR filter with cutoff at 700 Hz and stopband at 875 Hz (175 Hz transition bandwidth, −6 dB suppression at 787.5, maximal ripples in passband 2%) to remove aliasing effects. A high-pass zero-phase FIR filter with cutoff at 1 Hz and stopband at 0 Hz (1 Hz transition bandwidth, −6 dB suppression at 0.5 Hz, maximal ripples in passband 2%) was also applied to remove slow drifts from the SEEG signals. Additionally, we also used a band-stop FIR filter at 50 Hz and its harmonics to remove the power line interference (1 Hz band-stop width, 53 dB attenuation at center frequency, maximal ripples in passband 2%).

In addition, we identified time periods containing widespread artifacts or interictal epileptic events such as spikes, using the procedure described in (Arnulfo et al., 2015). Following this method, we used Morlet wavelets (width $m = 7$) to obtain a spectral decomposition of each signal into 33 logarithmically scaled frequencies from 2 to 512 Hz in steps of 1/4 octave. Then, we divided the signal envelopes in nonoverlapping 250 ms temporal windows. Corrupted temporal windows were defined as those where at least 10% of contacts had amplitude envelopes 5 standard deviations above their respective mean amplitude in more than half of the 33 frequency bands.

2.6 | Event-related potentials

Before conducting the spectral analysis, we analyzed the average signal across trials for a selection of relevant recording sites in each subject. For subject 1, our relevant contact was placed in V1/V2 (deepest electrode contact of the trajectory highlighted in Figure 1b). To compute the event-related potential (ERP) that was locked to the stimulus onset and avoid potential noise due the low number of trials, we further low-pass-filtered the data under 30 Hz (FIR filter with 6 dB suppression at 33.75 Hz, maximal ripples in passband 2%). We then epoched the data (−500 to 1500 ms from stimulus onset), baseline-corrected each epoch (subtraction of the mean across the baseline period, from −500 to 0 ms) and extracted the median across trials.

For subject 2, our relevant contact was placed in the left-hemisphere primary motor cortex (M1), approximately at the location of right-hand movement control. In this case, we extracted the ERP in M1 during recognized and nonrecognized trials, time-locked to button press or response timeout end, respectively. To compute the ERPs, we low-pass-filtered the data under 30 Hz, epoched the data (500 ms before stimulus presentation to 500 ms after button press or response timeout end, respectively), baseline-corrected each epoch (subtraction

of the mean across the baseline period, from −500 to 0 ms before stimulus presentation), aligned the data to button press or response timeout end, respectively, chunked each epoch from −500 to 500 ms from behavioral response and extracted the median across trials of each type (recognized vs. nonrecognized). In this case, we tested differences in the signals across both conditions using the following procedure. Experimental conditions were compared using a Ranksum test at each time point, with a criterion of $p < .05$ for a minimum of 102 consecutive samples (50 ms).

2.7 | Spectral estimates

Spectral power was estimated from 4 to 512 Hz using an adaptive multitaper method based on discrete prolate spheroidal sequences (DPSS, aka. Slepian sequences) (Mitra & Pesaran, 1999; Slepian & Pollak, 1961; Thomson, 1982). For our analysis, we used custom-made code to achieve the highest flexibility in adjusting the temporal and frequency smoothing for each frequency independently. Following this approach, we sought to find the best temporal resolution at lower frequencies, while obtaining more accurate power estimates at typically low SNR (signal-to-noise ratio) higher frequencies, at the expense of temporal and frequency resolution.

As suggested by previous literature (Buzsáki & Draguhn, 2004; Hipp et al., 2012), both the mean frequency and bandwidth of meaningful brain activity typically follow a logarithmic progression. Low-frequency activity (theta, alpha, beta) is thought to be oscillatory, frequency-specific, and less spatially localized, reflecting a sum of different contributions, in particular widespread postsynaptic potentials. On the other hand, high frequency activity (gamma, high-gamma and above) has a broadband profile and is typically thought to reflect locally synchronized neuronal activity. However, the specific frequency range of such activity is not well established and can vary depending on the recording technique (Buzsáki & Draguhn, 2004).

To consistently capture the specificities of low and high frequency activity, we computed power estimates across 29 logarithmically scaled frequencies f from 4 to 512 Hz in steps of 1/4 octave, that is, each frequency was obtained by multiplying the previous one by $2^{1/4}$. In addition, we adjusted the spectral smoothing parameter to match 3/4 octave, yielding a spectral resolution of $[f − 0.34f, f + 0.34f]$ for each frequency of interest f. Regarding the temporal resolution, we followed a different approach for frequencies above and below 32 Hz. For every frequency of interest f below 32 Hz, we adjusted time windows to include 6 cycles of f, using shorter windows for larger frequencies. This yielded a temporal smoothing ranging from $t \pm 750$ ms at 4 Hz to $t \pm 95$ ms at 32 Hz around each time point t for our estimates. With this temporal and frequency smoothing, we could use a total of three tapers for the spectral estimates at each frequency. In contrast, for frequencies above 32 Hz, we used a fixed temporal smoothing of ±100 ms around each time point (total temporal smoothing of 200 ms), which allowed us to use a greater number of tapers for larger frequencies (from 3 tapers at 32 Hz to 69 tapers at 512 Hz), thus increasing the signal-to-noise ratio of our spectral
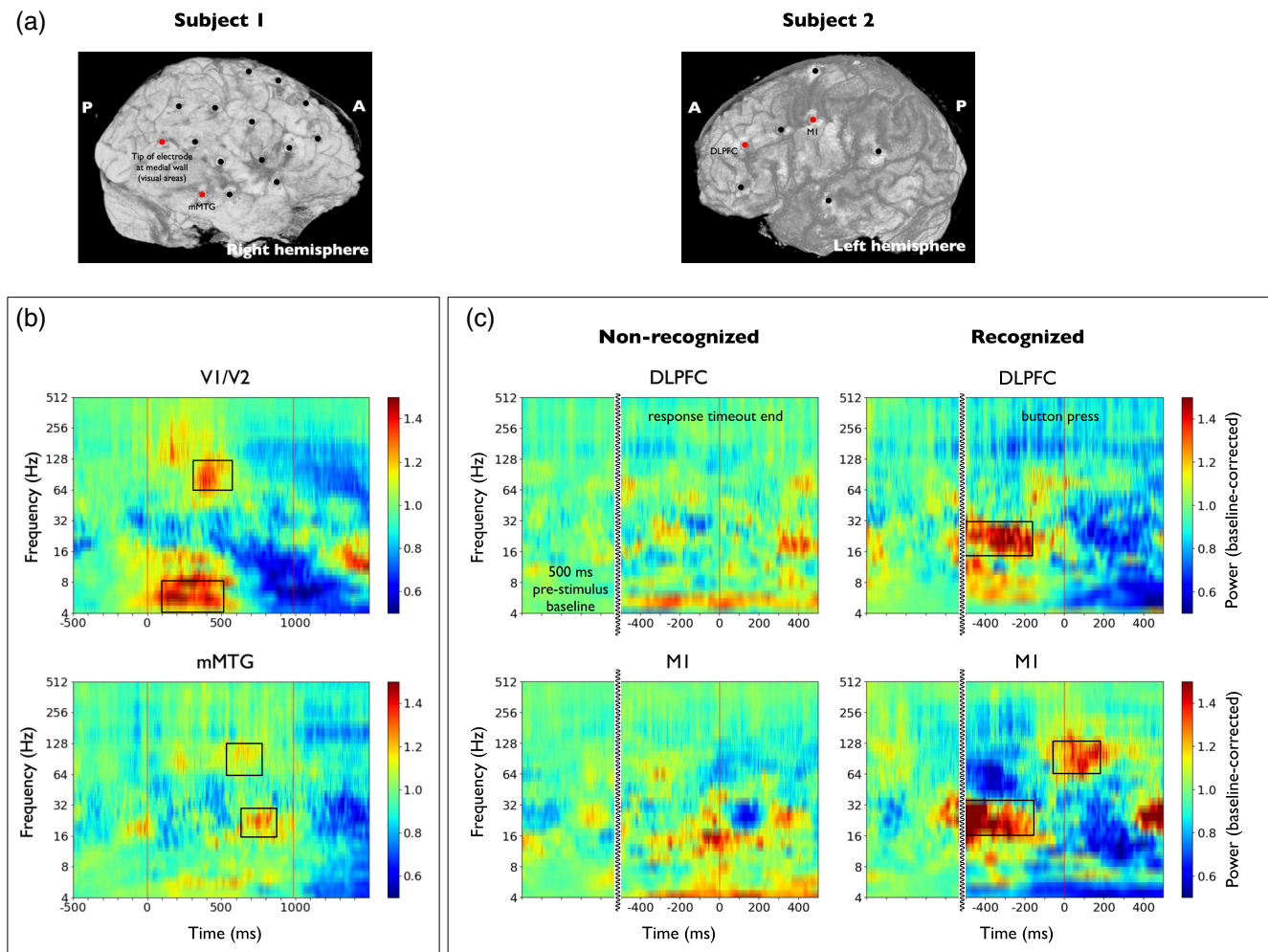
FIGURE 2 Spectral activations in different task-relevant ROIs for each subject. (a) 3D brain reconstructions showing the electrode entry points for subjects 1 and 2 (black and red dots). The full trajectory and end point of the electrode targeting V1/V2 in subject 1 can be seen in Figure 1b. Red dots highlight electrodes for which spectrograms are shown in (b) and (c). (b) Median across all trials of the baseline-corrected spectrograms aligned to stimulus presentation (0 ms) and obtained from two different key recording sites in the visual stimulus processing pathway of subject 1. The time–frequency windows of interest (TFOIs) used for statistical comparisons are marked with black rectangles. There is an early power increase in the theta band ($p < 10^{-5}$) in the visual cortex (V1/V2, same contact as in Figure 1c) followed by high-gamma discharges ($p < 10^{-5}$). In the mMTG (middle portion in the anterior–posterior axis of the middle temporal gyrus) we found power activations during the second half of the stimulus presentation both in the beta ($p < .001$) and the high-gamma range ($p < .001$). Vertical red lines indicate the stimulus onset and offset times, respectively. (c) Median baseline-corrected spectrogram of the single-trial LFP power across recognized and nonrecognized trials aligned to button press or response timeout end (0 ms, red vertical line), respectively, obtained from two different areas related to perceptual decision making and motor report. Power increases in the beta band until 250 ms before button press were found to be significant both in DLPFC (dorsolateral prefrontal cortex) and M1 (same contact as in Figure 1d) with respect to baseline distribution ($p < .01$), but not significant with respect to nonrecognized trials. A significant increase in high-gamma power was found in M1 around button press both with respect to baseline ($p < .01$) and to the nonrecognized trials ($p < .01$). Prestimulus baseline is also shown for comparison. Curvy lines mark a discontinuity in time

estimates. Independent power estimates were obtained by projecting the signals onto each taper. Then, single-taper estimates were averaged across tapers, thus obtaining a single power time course for frequency.

To avoid undesired boundary effects, we first obtained spectral estimates across the whole task period and epoched the data afterwards. For stimulus-related responses, we considered the epoch comprised from 500 ms before stimulus presentation to 1500 ms after stimulus presentation (this includes the stimulus period and a poststimulus period of at least 500 ms). Trial periods containing corrupted time windows as defined in Section 2.5 were discarded. For each trial, time–frequency plots were normalized at each scale by the mean power (division by the mean power at that scale) computed during the baseline period (from −400 to −100 ms, to avoid temporal contamination), as done in Rey et al. (2014). Then, we took the median across all trials to characterize each contact's response to the stimulus.

On the other hand, for motor-related responses (recognized and nonrecognized), we considered the epoch comprised from 500 ms before stimulus presentation to 500 ms after button press or response timeout end, respectively. For each trial, time–frequency plots were normalized at each scale by the mean power (division by the mean power at that scale) computed during the baseline period (from -400 to -100 ms, to avoid temporal contamination). We then aligned the data to button press or response timeout end, respectively, chunked each epoch from -500 to 500 ms from behavioral response and extracted the median across trials of each type (recognized vs. nonrecognized).

To validate our assumption that multitaper estimation might better capture local high-frequency activations than other temporally resolved techniques, we repeated the whole analysis using a wavelet approach, and compared the spectral power estimates. Power estimates were obtained between 4 and 512 Hz using the same 29 logarithmically scaled frequencies f as before with Morlet wavelets ($m = 7$). We then epoched, normalized and averaged the spectrograms exactly as we did with the multitaper estimates. In addition, we repeated the same analysis filtering the wavelet power estimates below 8 Hz before epoching and averaging, to obtain a similar temporal smoothing than with the continuous multitaper method. See Supplementary Information and Figure S1 for results and discussion.

2.7.1 | Statistical inference of task-related activations

When assessing stimulus-related activations, the median of the spectrograms obtained by means of multitaper power estimation was computed over all face presentation trials. Following (Rey et al., 2014), we visually identified time–frequency windows of interest (TFOIs) related to the stimulus presentation on the trial-median spectrograms of certain recording sites of interest (for instance, marked with black rectangles in Figure 2b). We then quantified the strength in the LFP power response in the defined TFOIs using the following nonparametric method. For each TFOI we defined a surrogate baseline TFOI (window spanning the same frequency ranges and time-width of the TFOI centered in the baseline period). For each trial, we extracted the mean power within the TFOI and the surrogate TFOI. We used a Ranksum test to evaluate significance of TFOI mean power against its surrogate baseline.

When assessing motor-related activations locked to the behavioral response (only subject 2), we computed the median of the spectrograms across the two conditions (recognized vs. nonrecognized) separately. In recognized trial-median spectrograms we visually identified time–frequency windows of interest (TFOIs) and tested the significance of their activations against the baseline period and against the nonrecognized trials independently. Significance with respect to baseline was tested using the procedure described in the previous paragraph. Significance with respect to nonrecognized trials was tested using a Ranksum test on TFOI mean power values between conditions.

2.8 | Global connectivity variables

To characterize the global connectivity state, we used two independent and complementary connectivity measures commonly used in the iEEG literature to quantify statistical relationships between signals: the functional connectivity (FC; Cruzat et al., 2018; Tauste Campo et al., 2018) and the phase-locking value (PLV; Axmacher et al., 2008; Arnulfo et al., 2015). On one hand, the functional connectivity (FC) is a linear measure based on amplitude correlations. It is computed as the Pearson correlation coefficient of signal time courses across time. On the other hand, the phase-locking value is a nonlinear measure based exclusively on phase couplings. It quantifies the consistency of phase differences between signal time courses across time. To avoid inflation of connectivity by spurious correlations generated by volume conduction, we considered all pairs of GM contacts, except those that were simultaneously in the same electrode and within the same ROI, since they typically measure very similar activity. Hence, only correlations between sufficiently distant contacts were taken into account. Note that in SEEG, the electrodes are placed only in some brain areas, which might vary from subject to subject. The mapping of neuronal connectivity is therefore limited to these areas, in contrast to connectivity across all cortical regions, as in fMRI or MEG.

2.8.1 | Time-resolved mean functional connectivity

We estimated the time-resolved functional connectivity (FC) between recording sites (broadband signals) using a sliding-window approach with a window length of 200 ms (410 samples) and a step of 1 sample. Before computing the FC, we high-pass filtered the signals above 5 Hz to have at least one full cycle within the 200-ms window (FIR filter with 6 dB suppression at 4 Hz, maximal ripples in passband 2%). When assessing the stimulus-locked global fluctuations, we aligned the signals' time courses to stimulus presentation, epoched the data from -500 to 1500 ms around stimulus onset and estimated the time-varying FC for a pair of signals using the following procedure. First, we computed the Pearson correlation coefficient between both signals in each time window and trial. For each time window, the FC between two contacts k_1, k_2 was computed as the magnitude of the average correlation value across trials:

$$FC_{k_1,k_2}(t) = \left| \frac{1}{N} \sum_{n=1}^{N} r_{k_1,k_2,n}(t) \right|,$$

where N is the number of trials and $r_{k_1,k_2,n}(t)$ represents the Pearson correlation coefficient between signals k_1 and k_2 in the time window starting at time t of the nth trial.

To summarize pairwise connectivity values into a single network metric, we defined the time-resolved mean FC (mFC) as the mean network strength, that is, the average of FC values over all connections (excluding pairs of contacts simultaneously in the same electrode and within the same ROI). Correlation values were Fisher's z transformed before taking averages across connections. With this procedure, we

obtained a single mFC value for each time window. For each subject, we visually identified one time window with a significant deflection of the mFC with respect to the baseline period and tested for significant differences using a Ranksum test across trials on the time average mFC in the baseline period and in the selected window, with a criterion of $p < .05$.

On the other hand, when assessing the motor-related global fluctuations, we selected recognized trials, aligned the signal's time courses to button press, epoched the data from -500 to 500 ms from button press and estimated the time-varying mFC using the procedure described before. We generated a surrogate mFC time-course using the nonrecognized trials. In this case, we aligned the signal's time courses to response timeout end, epoched the data from -500 to 500 ms from response timeout and estimated the time-varying mFC.

The main analysis was performed by computing the broadband mFC (Tauste Campo et al., 2018), that is, by estimating the Pearson correlation between broadband signals. Fluctuations captured by this measure might be explained by frequency-dependent correlations. To account for such effects, we also computed the mFC in the alpha (8–12 Hz), beta (12–30 Hz), gamma (30–70 Hz) and high-gamma (70–150 Hz) bands independently (see Figure S2). To do so, we computed the Pearson correlation between band-filtered signals using the same procedure described above.

2.8.2 | Time-resolved mean phase locking value

We estimated the time-resolved phase-locking value (PLV) between recording sites across 29 logarithmically scaled frequencies f from 4 to 512 Hz using the multitaper method with the same parameters and procedure specified in Section 2.7. For every frequency f below 32 Hz, we used a window length of $T = 6/f$ (6 cycles of f) and a step of 1 sample. For frequencies above 32 Hz, we used a window length of 200 ms and a window step of 1 sample. First, analytic signal estimates were obtained independently for each taper, frequency, and contact. Then, single-taper estimates were averaged across tapers and phase time courses were extracted from the taper-averaged analytic signals using the Hilbert transform. When assessing the stimulus-locked global fluctuations, phase signals were aligned to stimulus presentation and epoched from -500 to 1500 ms around stimulus onset. For each time window, the PLV between two contacts k_1, k_2 was computed as the magnitude of the average complex phase difference across trials (Lachaux et al., 1999):

$$\text{PLV}_{k_1,k_2}(f, t) = \left| \frac{1}{N} \sum_{n=1}^{N} e^{i\left(\phi_{k_1,n}(f,\ t) - \phi_{k_2,n}(f,\ t)\right)} \right|,$$

where N is the number of trials and $\phi_{k,n}(f, t)$ represents the phase estimate of contact k at frequency f and in the time window starting at time t of the nth trial. PLV ranges from 0 to 1, where 0 represents maximal phase variability and 1 represents perfect phase locking between signals.

Finally, the mean PLV (mPLV) was defined as the mean network strength, that is, the average of PLV values over all connections (excluding pairs of contacts simultaneously in the same electrode and within the same ROI). The mPLV was obtained for each time window and frequency, thus obtaining a frequency- and time-resolved global network metric.

To study motor-locked global responses, we computed the mPLV across the two sets of trials (recognized vs. nonrecognized), independently, as done for the mFC. In this case, phase signals were aligned to button press or response timeout end and epoched from -500 to 500 ms from button press or response timeout end, respectively. We then estimated the time-varying mPLV using the same procedure described above.

2.9 | Coupling between local activity and global connectivity fluctuations

To study local–global relationships, we aimed to have one time-varying variable $L_k(t)$ for each recording site k to capture local dynamics (derived from the spectrograms) and one global time-varying variable $G(t)$ capturing fluctuations in connectivity among recording sites (derived from either the mFC or the mPLV). Based on the preliminary visual inspection, we refined our definition of local activity and defined it as high-gamma activity (64–256 Hz). Hence, for each site, the local variable was defined as the average of its (median) spectrogram within the aforementioned high-frequency range. In contrast, at the global level, we used the mFC as defined in the previous section. We also defined a second global variable based on the the mPLV within the frequency range where it showed the highest stimulus modulation (6–16 Hz). To do so, we averaged this variable across the frequency range 6–16 Hz.

To assess the degree of correlation between each contact's local activity $L_k(t)$ and the global connectivity fluctuations measured by the proposed global variable $G(t)$, we used the following procedure. For each recording site k, we computed the Spearman correlation coefficient between its local variable and the global variable across the entire epoch $\rho_k = \rho(L_k(t), G(t))$, where $\rho(\cdot)$ stands for the Spearman correlation operator. To infer the significance of each estimation, we built the corresponding null distribution using circular shifts of the local variable, which preserved the local and global variables' autocorrelation properties (around 200 ms by definition) while destroying their temporal alignment. A detailed description of this methodology can be found in the Supplementary Information. Only medium and large effect size correlations ($r > 0.3$) were kept. In addition, significance level was set to $\alpha = 0.05$ and corrected for multiple comparisons using Bonferroni correction (number of contacts).

A similar procedure was used to assess local–global relationships in the motor-locked setting. In this case, local and global variables were aligned to button press, chunked in temporal windows from -500 to 500 ms, and only obtained for recognized trials. We then assessed the degree of correlation between each recording site's local

activity and the global connectivity fluctuations using the procedure described in the previous paragraph for the recognized trials.

2.10 | Data and code availability

Due to institutional restrictions, the data that supports the findings of this study can be accessed only with a data sharing agreement. All code used in this work can be found at https://github.com/mvilavidal/localglobal2022.

3 | RESULTS

3.1 | Implantation, behavioral task and basic ERP analysis

We applied our method to the intracranial EEG signals from subjects 1 and 2 while they performed a face-recognition task (Figure 1a). In this task, each trial consisted of a short prestimulus baseline period, an image presentation period and a poststimulus period in which the subject was instructed to respond within a maximum allowed time.

Subject 1 had 16 electrodes implanted, accounting for a total of 175 contacts, among which 47 were selected for further analysis (see Table 1 and Figure 1b). Electrodes were implanted on the left hemisphere and covered the primary or secondary visual cortex (1 electrode in V1/V2), the supramarginal gyrus (2 electrodes), large portions of the lateral aspect of the temporal lobe (5 electrodes in the anterior and posterior regions of the STG, MTG, and ITG), anterior and posterior parts of the hippocampus (2 electrodes), the cingulate cortex (4 electrodes distributed uniformly from its rostral anterior to its posterior aspect close to the isthmus), and to a lesser extent the frontal lobe (1 electrode in M1, 1 in the lateral aspect of the PMC and 2 in the DLPFC). For connectivity analyses, we considered all pairs of GM contacts, except those located in the same electrode and within the same ROI, accounting for a total of 1031 pairs. Subject 1 completed $N = 64$ trials that lasted approximately 12 minutes. Around 0.2% of inspected time windows were marked as corrupt (7/2880). However, none of them affected analyzed periods (from -500 to 1500 ms around stimulus onset) and no trials were discarded. ERP in the visual cortex of subject 1 was found to be modulated by the stimulus presentation (Figure 1c), showing negative peaks of $-40\,\mu V$ at around 150 ms after stimulus presentation, with a progressive increase to $50\,\mu V$ at 500 ms after stimulus presentation.

Subject 2 had 7 electrodes implanted, with a total of 93 contacts, among which 26 were selected for further analysis (see Table 1). Implanted electrodes covered large portions of the frontal lobe (1 electrode in M1, 1 in the medial aspect of the PMC, 2 in the DLPFC and 1 in the VLPFC), the cingulate cortex (5 electrodes distributed from its anterior to its posterior aspect), the STG (2 electrodes) and the insula (1 electrode). For connectivity analyses, we considered all pairs of GM contacts, except those located in the same electrode and within the same ROI, accounting for a total of 307 pairs. Subject 2 completed

$N = 71$ trials that lasted approximately 5 min. Around 0.3% of inspected time windows were marked as corrupt (3/1200). As before, none of them affected analyzed periods (from -500 to 1500 ms around stimulus onset; from -500 to 500 ms around button press or response timeout) and no trials were discarded. Among all pictures, 22 were reported as recognized, while 49 were reported as nonrecognized. In subject 2, event-related potential (ERP) in right-hand M1 (Figure 1d) displayed significant differences between conditions from -273 to -214 ms before button press and from 4 to 189 ms after button press (Ranksum test at each time point and across conditions, with a criterion of $p < .05$ for a minimum of 102 consecutive samples, 50 ms).

3.2 | Detection of task-driven local activity

The spectrogram of each signal was obtained using the multitaper method. Power estimates at each frequency were then epoched and expressed as a fraction of the mean power during the baseline period (from -400 to -100 ms from stimulus onset) at each frequency, for each trial separately (see Section 2.7).

Subject 1 had an implantation that largely covered the stimulus processing pathway (Figure 2a, left panel): V1/V2, ITG, MTG, hippocampus. In this case, we studied stimulus-related activations across all trials and disregarded behavioral responses (see Section 2.2). For every contact, the median of the spectrograms was computed over all face presentation trials. Figure 2b shows the spectrograms of two contacts of subject 1 monitoring V1/V2 and the middle portion (anterior–posterior axis) of the MTG (mMTG) that displayed significant power activations. In V1/V2, we found that the brain responses to the presentation of the stimulus were characterized by an increase in the theta band immediately after the stimulus onset time (100–500 ms, 4–8 Hz, $p < 10^{-5}$) and a high-gamma increase after 300 ms (300–600 ms, 64–128 Hz, $p < 10^{-5}$). In addition, the mMTG exhibited a significant deflection localized in the beta band during the second half of the stimulus period (16–32 Hz, 600–900 ms, $p < .001$), accompanied by a more diffuse activation in the high-gamma range (64–128 Hz, 500–800 Hz, $p < .001$).

In subject 2, no ROI directly related to visual stimulus processing was monitored, while various areas related to perceptual decision making and motor report were covered (Figure 2a, right panel): M1 at the position of the right-hand (used for button pressing), premotor areas, VLPFC and DLPFC. We first performed the stimulus-related analysis. Here, we also studied motor-related activations in recognized trials. For every recording site, the median of the spectrograms was computed over each set of trials aligned to button press or response timeout end, respectively (see Figure 2c). In this setting, we found significant power activations in the beta band of the the DLPFC before button press (Figure 2c, 16–32 Hz, from 500 to 250 ms before button press, $p < .01$). These power activations were, nonetheless, nonsignificant when compared to nonrecognized trials. Significant beta power activations were also found in the same time–frequency band in the primary motor cortex (16–32 Hz, from 500 to 250 ms before button
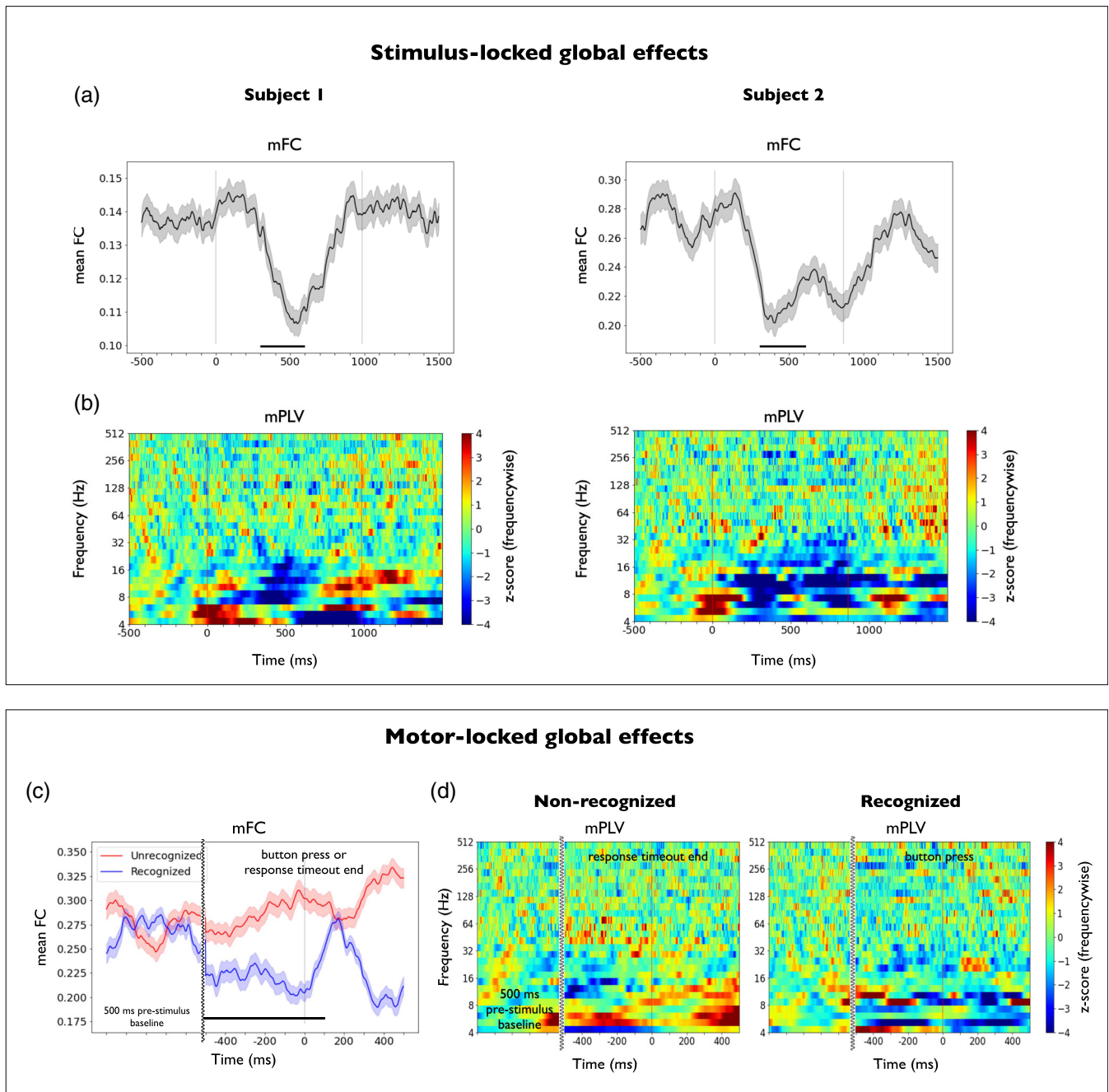
FIGURE 3 Legend on next page.

press, $p < .01$). These were also nonsignificant when compared to nonrecognized trials. In addition, M1 displayed high-gamma activations around button press (64–128 Hz, from 50 ms before to 200 ms after button press). Unlike the previous cases, the activations here were significant when compared both to the baseline period ($p < .01$) and to the nonrecognized trials ($p < .01$).

Overall, the detected ROIs at early and late stages of the cortical face recognition and report pathway, that is, V1/V2 and M1, provided statistical evidence of activations at frequency ranges (Buzsáki et al., 2012) and times (Salinas & Romo, 1998; Van Vugt et al., 2018) that were compatible with local activity encoding visual stimulus and

motor report information. Based on these results, we chose to define the local variables of the local–global analysis within the frequency range 64–256 Hz.

3.3 | Global connectivity effects of stimulus presentation and motor response

The mean functional connectivity (mFC) and the mean phase locking value (mPLV) were computed as described in Methods (see Section 2.8). The upper panel of Figure 3 shows the time evolution of

both variables in the stimulus-locked setting for each subject (Figure 3a, mFC; Figure 3b, mPLV). Despite having different implantation schemes, a decrease in the mFC associated to stimulus presentation was consistently found in both subjects with respect to their prestimulus baseline distribution in a temporal window of 300–600 ms. To test significance, a Ranksum test was applied across contact pairs on the average FC in the baseline period and the 300–600 ms window ($p < 10^{-6}$, Cohen's d effect size $d > 5$ in both subjects, Figure 3a). Figure S2 shows the time evolution of mFC when computed in the physiological bands. The broadband mFC decrease was found to be localized in the alpha (8–12 Hz) and, to some extent, beta bands (12–30 Hz). This decrease in time-resolved mFC (time windows of 200 ms) was accompanied by a concurrent decrease in mPLV in the frequency range 6–16 Hz that lasted 200 ms (z-score < -3, Figure 3b).

To show that the reported connectivity effect was of widespread nature we performed two control analysis. First, we inspected the influence of power fluctuations into the mFC and mPLV decreases. For mFC, we plotted the time-resolved average standard deviation and covariance across all contact pairs in the same period (see Figure S3) paying special attention at the 300–600 ms window after stimulus onset. The curves illustrate that a prominent decrease was manifested for both subjects in their average covariance (Figure S3b) while only mild increases were observed in the average standard deviation, that is, in the power amplitude of the signals (Figure S3c), suggesting that the observed mFC decay did not result from mere power fluctuations and reflected a real decrease in connectivity. For mPLV, we assessed whether the decrease in 6–16 Hz was due to phase decoupling or simply reflected a decrease in power. To do so, we compared the average time/frequency power with the mPLV (Figure S4). No global decrease in energy was observed. Hence, the decay in mPLV could not be explained by a decrease in the signal-to-noise ratio

or a simple decrease in power in 6–16 Hz. This suggests that a genuine phase decoupling in this frequency range. Second, we assessed how the connectivity decay in both variables varied across all contacts (see Figures S5 and S6). Indeed, Figures S5b and S6b suggest that the period 300–600 ms was affecting the connectivity strength of a substantial subset of recording contacts (see marked rectangles) while the curves for prestimulus and stimulus epochs displayed in Figures S5c and S6c confirmed that the decay was a generalized effect across the implantation scheme of both subjects. In addition, the connectivity matrices shown in Figure S7 highlight that the decay is distributed over a great proportion of contact pairs.

With regard to the motor-locked setting, the lower panel of Figure 3 shows the time evolution of the two global variables for subject 2. In this setting, trials were aligned to button press or response timeout end, and global variables were computed in a time period from −500 to 500 ms across recognized ($N = 22$) and nonrecognized ($N = 49$) trials, respectively (Figure 3c, mFC; Figure 3d, mPLV). A significant mFC difference between conditions was found between 500 ms before and 100 ms after button press or response timeout end, respectively (Ranksum test applied across contact pairs on the average FC in the selected time window and across conditions, $p < 10^{-6}$, Cohen's d effect size $d > 5$). Here, no significant differences with respect to the prestimulus baseline or across conditions were found with mPLV in the frequency range 6–16 Hz.

3.4 | Local–global relationships

We here investigated the relationship between the local variable of each recording site (average power across the high-gamma range, 64–256 Hz) and the two global connectivity-based variables (mFC, and mPLV averaged across the range 6–16 Hz). This relationship was

FIGURE 3 Stimulus- and motor-related global effects. The upper panel shows the temporal evolution of the global variables aligned to stimulus presentation in subjects 1 and 2. (a) Time course of the broadband mean functional connectivity (mFC) aligned to stimulus onset. Mean ± SEM across all GM contact pairs ($N_{\text{pairs}} = 1031$ in subject 1, $N_{\text{pairs}} = 307$ in subject 2). Correlation values were Fisher's z transformed before taking averages across contacts pairs. See Section 2.8, for details. Vertical dark lines indicate the stimulus onset and offset times, respectively. A significant decrease in the mFC associated to stimulus presentation was found in the two subjects with respect to their prestimulus mean mFC value (300–600 ms, marked with black bars, Ranksum test applied across contact pairs on the average FC in the baseline period and the 300–600 ms window, $p < 10^{-6}$, Cohen's d effect size $d > 5$ in both subjects). (b) Time-resolved mean phase locking value (mPLV) aligned to stimulus presentation. See Section 2.8, for details. Plots have been z-scored with respect to the prestimulus period (from −500 to −100 ms) at each frequency scale for visualization purposes. Vertical red lines indicate stimulus onset and offset times, respectively. A significant phase-decoupling was consistently observed across trials in the frequency range 6–16 Hz around 300 ms after stimulus presentation in the two subjects (z-score <3). This effect lasted around 200 ms. The lower panel shows the evolution of the global variables aligned to the behavioral response across the corresponding set of trials in subject 2. (c) Time course of the broadband mean functional connectivity (mFC) for subject 2 in recognized ($N = 22$) and nonrecognized ($N = 49$) trials. Mean ± SEM across all GM contact pairs ($N_{\text{pairs}} = 307$) for each set of trials aligned to button press or response timeout end (marked with a vertical dark line), respectively. Prestimulus baseline is also shown for comparison. Curvy lines mark a discontinuity in time. A significant mFC difference between conditions was found between 500 ms before and 100 ms after button press or response timeout end, respectively (marked with a black bar, Ranksum test applied across contact pairs on the average FC in the selected time window across conditions, $p < 10^{-6}$, Cohen's d effect size $d > 5$). (d) Time-resolved mean phase locking value (mPLV) for subject 2 in recognized ($N = 22$) and nonrecognized ($N = 49$) trials, aligned to button press or response timeout end, respectively. Plots have been z-scored with respect to the prestimulus period (from −500 to −100 ms before stimulus presentation) at each frequency scale for visualization purposes. Vertical red lines indicate button press or response timeout end, respectively. Prestimulus baseline is also shown for comparison. Curvy lines mark a discontinuity in time. No significant differences could be found between both conditions in the frequency range 6–16 Hz around button press / response timeout end
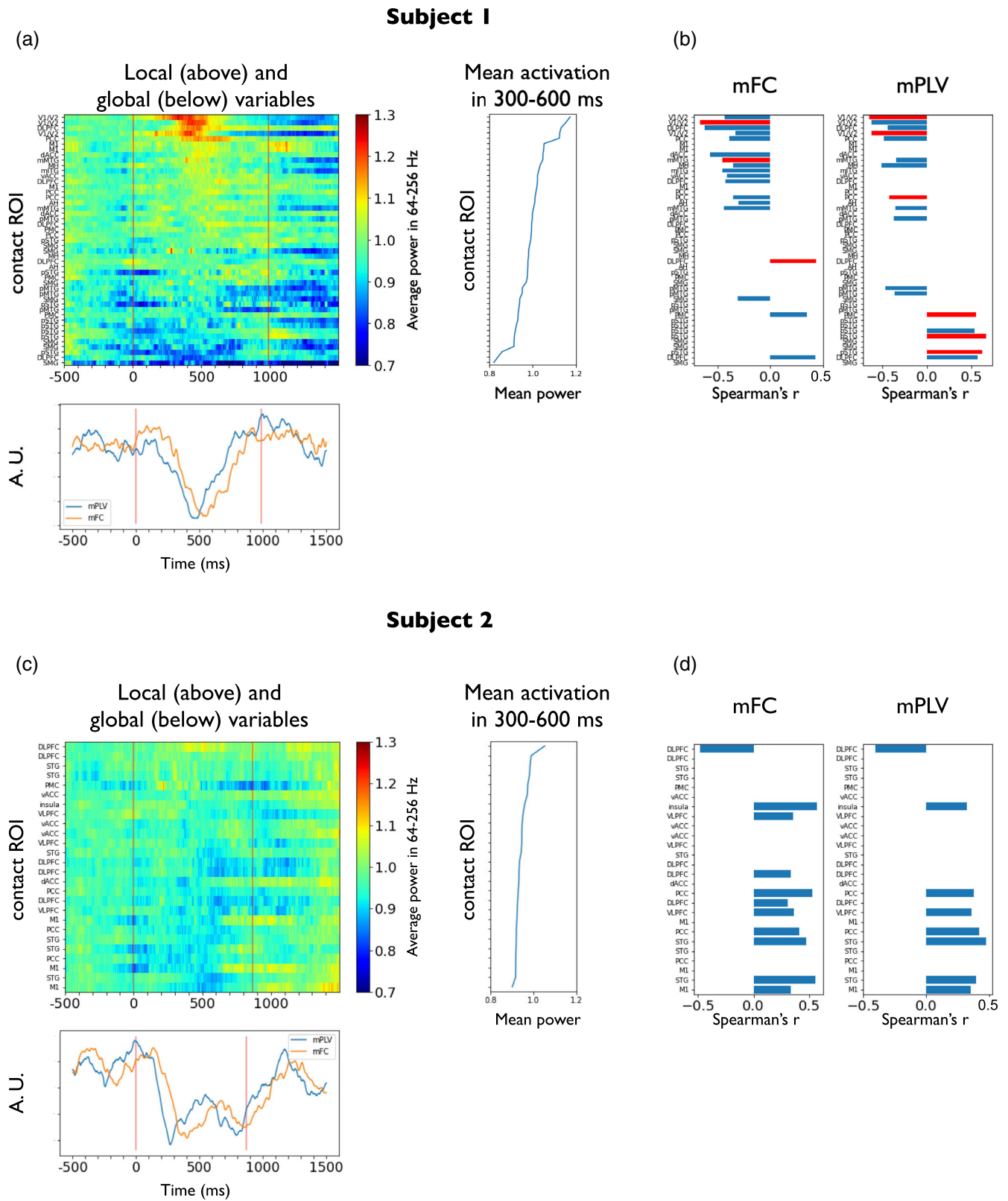
Subject 1

(a)

(b)

Subject 2

(c)

(d)

FIGURE 4 Legend on next page.

explored in the two proposed settings (stimulus-locked, motor-locked) to find potential local–global couplings associated to stimulus information processing and motor reports (see Section 2.9).

3.4.1 | Stimulus-locked local–global coupling

Figure 4 shows the results for the stimulus-locked local–global analysis in subjects 1 (Figure 4a,b) and 2 (Figure 4c,d). In particular, the upper left plot in Figure 4a shows the time evolution of each contact's local variable (average power across the high-gamma range, 64–256 Hz) across the stimulus presentation in subject 1. Contacts were sorted by the mean high-gamma power in the 300–600 ms time window after stimulus presentation, which defines the task-related activation of each recording site (shown right, next to each contact's power evolution). The lower plot in Figure 4a shows the time evolution of the two global variables (mFC, and mPLV averaged across the range 6–16 Hz) temporally aligned to the local variables. The results of local–global testing are shown in Figure 4b for each global variable, separately. To assess the degree of local–global correlation we computed the Spearman correlation coefficient between each local variable and the global variable across the entire epoch. Only medium and large effect-size correlations ($r > 0.3$) were considered. Significance level was set to $\alpha = 0.05$ (null distribution built using circular shifts of the local variable) and corrected for multiple comparisons across multiple contacts. In subject 1, the local increase of activity of high-gamma activity at V1/V2 was found to have a significant correlation of -0.7 with the decrease in the two global variables (see examples of downsampled scatter plots for each global variable in Figure S8a). The decrease of mFC was also significantly correlated with high-gamma activations in other contacts such as mMTG (middle portions of the MTG, $r \approx -0.5$), which also ranked high in task-related activations. The fluctuations in mPLV correlated also with other contacts that were less active during the task. A significant negative correlation was found with the PCC. In addition, some contacts that exhibited negative deflections in high-gamma activity correlated positively with mPLV fluctuations (PMC, posterior portion of the STG, $r \approx 0.5$).

In an analogous form, the upper left plot in Figure 4c shows the time evolution of the local variable (average power across the high-gamma range, 64–256 Hz) across the stimulus presentation in subject 2. High-gamma activity appears to be much less modulated by the task than in subject 1 (see task-related activation of each recording site next to each contact's power evolution), probably due to an implantation scheme covering regions that were not involved in the initial processing of visual stimuli. The lower plot in Figure 4c shows the time evolution of the two global variables (mFC, and mPLV averaged across the range 6–16 Hz) temporally aligned to the local variables. The results of local–global testing are shown in Figure 4d for each global variable, separately. Interestingly, although global fluctuations in subject 2 exhibited very similar trends to those observed in subject 1, no local variable significantly explained the reported fluctuations.

3.4.2 | Motor-locked local–global coupling

We here tested couplings between the global variables and the local ones when aligned to button press (time period from -500 to 500 ms from motor report) in subject 2. Figure 5 shows the results for motor-locked local–global analysis in recognized trials. The upper left plot in Figure 5a shows the time evolution of each contact's local variable (average power across the high-gamma range, 64–256 Hz) around the motor report in subject 2. Contacts have been sorted by the mean high-gamma power from -100 to 200 ms from button press, which defines the motor-related activation of each recording site (shown next to each contact's power evolution). The lower plot in Figure 5a shows the time evolution of the two global variables (mFC, and mPLV averaged across the range 6–16 Hz) temporally aligned to the local variables. In all figures, prestimulus baseline is also shown for comparison although not used for local–global analysis. Local–global correlation was assessed using the same procedure as in the stimulus-locked setting. The results of local–global testing are shown in Figure 5b for each global variable, separately. Importantly, local increases in activity at M1 were found to be positively correlated ($r = 0.5$, $p < .05$ corrected for multiple comparisons across contacts;

FIGURE 4 Stimulus-locked local–global coupling for subjects 1 (upper panel: subfigures a and b) and 2 (lower panel: subfigures c and d). (a) Local and global variables for subject 1. (Upper) local variable for each brain recording site in subject 1 (median spectrogram power across all trials, averaged across the high-gamma range, 64–256 Hz, see Section 2.9). Vertical red lines indicate the stimulus onset and offset times, respectively. Contacts have been sorted by the mean high-gamma power in the 300–600 ms time window after stimulus presentation, which defines the task-related activation of each contact (shown next to each contact's power evolution). (Lower) global variables: mFC, and mPLV averaged within the frequency range 6–16 Hz. Global variables have been rescaled for the purpose of comparison (shown in arbitrary units, A.U.). Vertical red lines indicate the stimulus onset and offset times, respectively. (b) Spearman correlation coefficient between each local variable and each global variable in subject 1. Correlations have been thresholded at medium-size effects ($r > .3$). In addition, significance was tested using a surrogate distribution via circular shifts, with a significance criterion of $\alpha = 0.05$ and corrected for multiple comparisons for the number of contacts. Significant correlations are indicated with red bars. Local increase in activity at V1/V2 appears to have a significant correlation of -0.7 with the decrease in the two global variables. In addition, the decrease in mFC seems to have a significant correlation with local activity in task-relevant contacts such as mMTG and mITG (middle portions of the MTG and ITG, respectively). The local activity at PCC appears to be negatively correlated with mPLV. (c) Local and global variables for subject 2. Analogous to (a). (d) Spearman correlation coefficient between each local variable and each global variable for subject 2. Analogous to (B). In this case, none of the local variables showed a significant correlation with the global variables
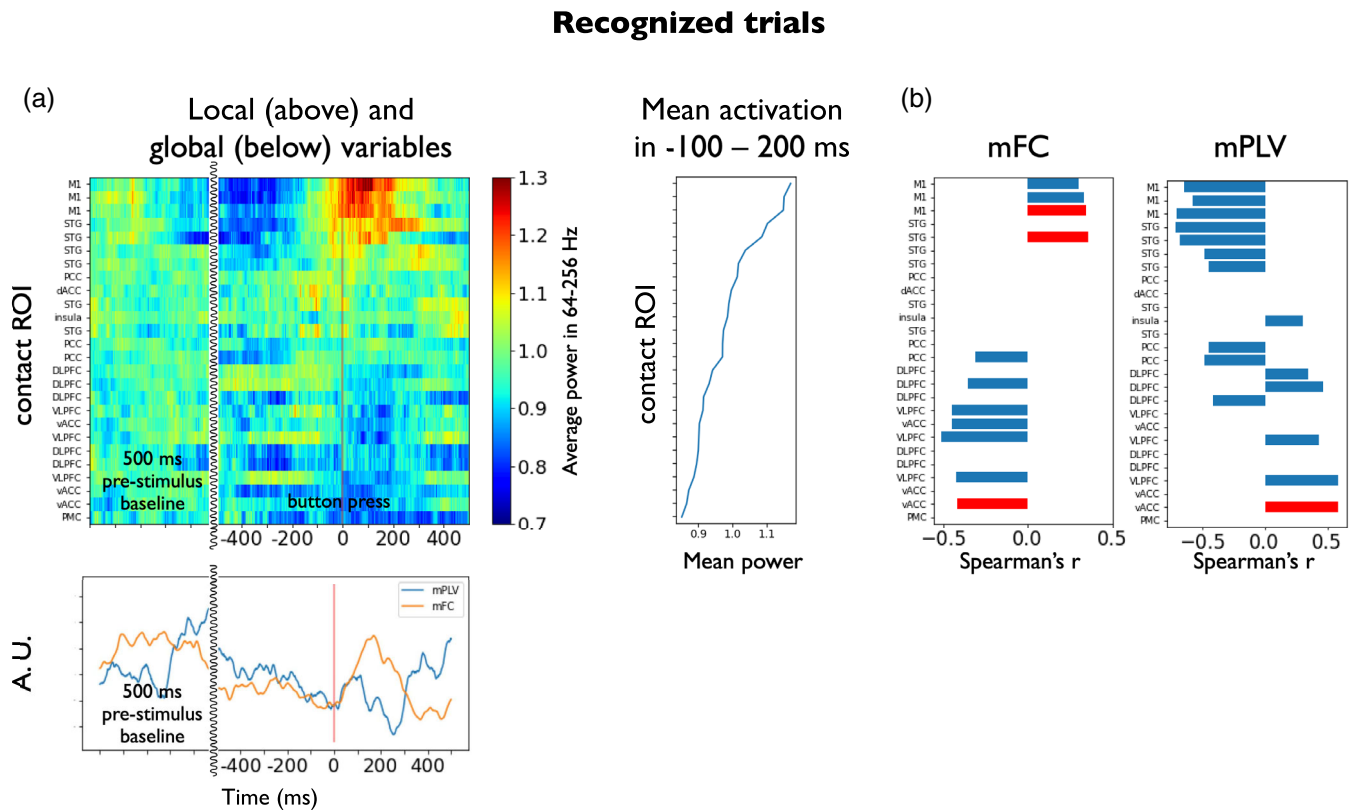
Recognized trials

FIGURE 5 Motor-related local–global coupling for subjects 2 in recognized trials. (a) Local and global variables for recognized trials. (Upper) local variable for each brain recording site in subject 2 aligned to motor report (median spectrogram power across recognized trials aligned to button press, averaged across the high-gamma range, 64–256 Hz, see Section 2.9). The vertical red line indicates button press. Contacts have been sorted by the mean high-gamma power in a time window around button press (from −100 to 200 ms), which defines the motor-related activation of each contact (shown next to each contact's power evolution). (Lower) global variables: mFC, and mPLV averaged within the frequency range 6–16 Hz. Global variables have been rescaled for the purpose of comparison (shown in arbitrary units, A.U.). The vertical red line indicates button press. Prestimulus baseline is also shown for comparison (not used for correlations). Curvy lines mark a discontinuity in time. (b) Spearman correlation coefficient between each local variable and each global variable in the recognized trials during the time period of −500 to 500 ms around button press. Correlations have been thresholded at medium-size effects (r > .3). Significance was tested using a surrogate distribution via circular shifts, with a significance criterion of $\alpha = .05$ and corrected for multiple comparisons for the number of contacts. Significant correlations are indicated with red bars. Local increase in activity in one contact located in M1 has a significant positive correlation of .5 with mFC. An additional contact in the STG appears to have a significant positive correlation with mFC. A contact in the vACC shows significant correlations both with mFC and mPLV, but its power fluctuations in the high-gamma range are much lower than those of M1

see an exemplary downsampled scatter plot in Figure S8b left) with mFC, that also exhibited an increase during motor report. One contact in the vACC that showed prominent negative deflections during the motor report period appeared to have significant negative correlations with mFC. This contact also displayed a significant correlation with mPLV. Taken together, the results for both subjects suggest the existence of a physiological link between the stimulus and motor-driven activity modulation of certain areas and slow global connectivity fluctuations.

3.5 | Additional analysis

We cross-validated the methodology in a third subject that performed a cognitive task under a slightly different paradigm (see Section 2.2) and compared the outcomes of the analysis with our previous

findings. First, we observed neural activations in the gamma and high-gamma bands around 300 ms after stimulus presentation in relevant contacts localized in the vicinity of V1/V2 (see Figure S9a left, 300–600 ms, 64–128 Hz, $p < 10^{-3}$) similarly to subject 1 (Figure 2a). In addition, high-gamma activity was detected in the anterior hippocampus starting 500 ms after stimulus presentation (Figure S9a right, 500–1000 ms, 64–128 Hz, $p < 10^{-4}$).

In the stimulus-locked setting, a consistent decay in global connectivity was observed after stimulus presentation. Although the mFC exhibited high baseline fluctuations that yielded a nonsignificant output (Figure S9b left), the connectivity decay present in subjects 1 and 2 (Figure 3b) was clearly captured by the mPLV as a phase decoupling within the frequency range 6–16 Hz. Accordingly, local–global coupling analysis was performed with mPLV (Figure S9d,e), which was found to be strongly modulated by the task. Indeed, local increases in activity at V1/V2 and STG contacts, respectively, were found to

negatively correlate with the decrease in mPLV ($r \approx -0.6$). In addition, the activity increase in AH during the second half of the stimulus presentation was coupled with enhanced global synchronization.

This third subject was also analyzed under the motor-locked setting. Specifically, subject 3 performed a total of 96 trials, from which 45 were reported as recognized and 51 as not recognized. Concordant with subject 2 (Figure 3c), a mFC difference between conditions was found between 500 ms before and 100 ms after button press or response timeout end, (Figure S9c left panel, Ranksum test applied across contact pairs on the average FC in the selected time window across conditions, $p < .05$, Cohen's d effect size $d > 2$). An increase in mFC after button press concordant with subject 2 was also found. In a similar vein, the mPLV signatures of recognized and nonrecognized trials up to 16 Hz (Figure S9c middle and right panels) also resembled those from subject 2, exhibiting a slight upper shift in the frequency range (see Figure S9c). Despite the lack of specific (i.e., contra-lateral to the moved hand) motor-related areas here, both global variables were found to correlate with the local activity of multiple potentially task-engaged areas, such as left MTG, ITG, insula and temporal pole.

4 | DISCUSSION

In this study we developed and systematized a methodological pipeline integrating neuroanatomic information, signal processing functions and connectivity measures to statistically infer potential correlations between the local activity and global connectivity fluctuations. This new local–global framework was defined and tested in two patients with drug-resistant epilepsy with iEEG recordings that performed a face-recognition task. Data from a third subject that performed a cognitive task under a slightly different paradigm was further analyzed to cross-validate some of our method's assumptions and previous findings with an independently generated dataset. With a small sample size, this study has a methodological conception and its main aim is to present a novel analytical framework to assess local–global couplings in iEEG recordings. The reported biological results should be regarded as a preliminary small-sample size application towards the developed concept.

The crucial point of our framework is the appropriate definition of local and global variables, and their accurate estimation. For the local variables, we used power activations in the high-gamma range (64–256 Hz) estimated via the continuous multitaper method, which is designed to reduce bias with respect to true spectral content (see Supplementary Information for a comparison and discussion of multitaper and wavelet estimation techniques). The global variables were defined by means of functional connectivity analysis. Crucially, they were based on lower frequency cofluctuations, which are thought to have a more widespread origin (Pesaran et al., 2018), reflecting more global states. Based on these premises, we made use of two independent functions in the low-frequency range to measure the brain sites' coupling consistency across time. On one hand, the mean functional connectivity (mFC) is based on temporal correlations between pairs of broadband signals and captures temporal cofluctuations across

recording sites. On the other hand, the mean phase-locking value (mPLV) relies on phase estimation and quantifies the consistency of phase differences between signal time courses (at each frequency). Then, local–global relationships were tested via correlation-based tests, although more sophisticated methods could also be used, as discussed in Section 4.4.

4.1 | Implantation and task analysis

Despite performing the same task, subjects 1 and 2 had differentiated implantation schemes, which allowed to test our framework with complementary conditions. Overall, ROIs at both ends of the cortical pathway in visual perception and motor report were covered when considering both subjects together. Implantation of subject 1 (Figure 1b) covered extensively the occipital and temporal lobes, including crucial areas of the cortical pathway in visual face perception and processing (V1/V2, ITG, MTG, hippocampus) (Bernstein & Yovel, 2015; Jonas et al., 2016; Wang et al., 2016), while implantation of subject 2 (Figure 2b) was more extense in the PFC, and motor and premotor areas. Primary results were obtained by aligning trials to stimulus presentation. In addition, we explored modulations aligned to motor-response in recognized trials. Subject 2 was particularly interesting for the purpose of motor-locked analysis, since one contact was located in M1 (left hemisphere), approximately in the region controlling right-hand movement, with which motor reports were made. In this contact, ERPs exhibited a significant deflection when compared to the nonrecognized trials locked to response timeout end.

4.2 | Task-driven activations

Following (Rey et al., 2014), we defined certain time–frequency windows of interest (TFOI) in the spectrograms of preselected key recording sites and tested whether activations in those windows were significant with respect to the prestimulus presentation or across conditions when aligned to motor response (Figure 2). Following this approach, in subject 1 we observed significant power increases in V1/V2 in the theta and and high-gamma range during the first half of the stimulus, that were followed by more diffuse activations in the MTG in the beta and high-gamma range during the second half of the stimulus period. Similar activations in the vicinity of V1/V2 in gamma and high-gamma ranges were also observed in subject 3. In this case, additional high-gamma activity was observed in the anterior hippocampus during the second half of the stimulus presentation (starting 600 ms after stimulus presentation). In subject 2 we found significant power activations across all trials in the beta band in the DLPFC and M1 during the second half of the stimulus presentation period. When aligned to motor responses, power activations in the high-gamma range emerged around button press in recognized trials for subject 2.

The above results generalize findings from previous literature related to the face perception pathway found with different recording modalities (Dobs et al., 2019; Grill-Spector et al., 2017; Landi &

Freiwald, 2017; Rey et al., 2014, 2015; Wang et al., 2016; Zhen et al., 2013) and help reconstruct additional stages of the visual processing pathway needed to consciously recognize face identities and of the motor planning pathway needed to engage in behavior. Interestingly, both ends of the cortical pathway (V1/V2 and M1) showed broadband high-frequency activity during stimulus presentation and perceptual report which might reflect the presence of neural populations encoding sensory and motor information in each area, respectively (Buzsáki & Draguhn, 2004). In contrast, intermediate nodes of this pathway such as the MTG area, engaged in processing visual face features, and the DLPFC, engaged in decision planning, exhibited prominent activity in the beta band during the second half of the stimulus presentation. In particular, beta activity in M1 across all trials not concurrent to high-gamma activity might reflect afferent potentials that do not result in local activity.

The encoding of visual stimuli in the visual cortex (Graf et al., 2011; Kohn & Smith, 2005; Smith & Kohn, 2008) and the neural correlates of the somatosensory-motor pathway (Tauste Campo et al., 2015; Luna et al., 2005; Romo et al., 2002; Salinas & Romo, 1998; Thura & Cisek, 2014) have long been studied in primates. The novelty of our study, however, lies in having been able to generalize previous results in human brain recordings. In addition, global fluctuations potentially reflecting cognitive states have been poorly analyzed due to the difficulty of recording simultaneous single neurons during task performance. Intracranial electroencephalography (iEEG) recordings from the human brain provide an opportunity to study such fluctuations at the global scale thanks to their coverage of brain areas so distant such as V1 and M1.

4.3 | Common global fluctuations independent of implantation scheme: preliminary findings

To characterize global connectivity states during the task, we used two complementary variables. On one hand, the mean functional connectivity (mFC) was defined as the average Pearson correlation across contact pairs in 200 ms time windows, thus capturing cofluctuations of the broadband signals (1–700 Hz), which are ultimately dominated by low frequencies. On the other hand, the mean phase-locking value (mPLV) was defined to characterize the consistency of phase differences between signal time courses at each frequency scale. Significant modulations associated to stimulus presentation in this variable were only found in the 6–16 Hz range. We therefore restricted our analyses to this frequency range for this variable.

Remarkably, despite having differentiated implantation schemes, the connectivity functions consistently showed in both subjects a significant global desynchronization occurring a few hundred milliseconds after stimulus onset (Figure 3, upper panel), which was shown to be of generalized nature and not specifically biased by power fluctuations (see Figures S3–S6). In line with these findings, a decay in connectivity was also observed after stimulus presentation in subject 3. Although the mFC exhibited very noisy fluctuations (Figure S9b left) the effect was clearly captured as a phase decoupling in the

frequency range 6–16 Hz measured with mPLV (Figure S9b right). This suggests that low frequencies in the monopolar montage might be useful when aiming to capture global connectivity states that are independent of the implantation scheme, as already implied by previous works (Tauste Campo et al., 2018). The decrease in time-resolved mFC reflects that the stimulus breaks baseline connectivity cofluctuations, owing to a potential specialization or segregation of different subnetworks in processing the incoming information. This decrease was localized in the alpha and beta bands (Figure S2), consistently with the results found with mPLV. Note that in our study we used different faces in each trial. Further studies should test whether the trial specificity is maintained when using exactly the same stimulus across trials. When studying motor-locked global effects (subject 2, Figure 3, lower panel), no clear trend was observed in the mPLV, while the mFC exhibited a transient increase after the response time, an observation that was reproduced in subject 3.

Due to the small sample size and diversity of implantation schemes, these observations should be taken as preliminary results towards the developed concept, in particular considering the large intersubject and interareal variability of oscillatory signals. Further studies should be performed to assess the consistency of reported results with more subjects and with more trials of each kind. We hypothesize that the stimulus presentation might initially trigger a specialization of the whole-brain network (reflected in the decrease of mFC and mPLV) to process the incoming stimulus in a segregated manner, followed by an increase in connectivity (reflected by the positive deflection in mFC around response) needed to integrate information and plan an internal response. Yet, the underlying mechanism behind the reported global fluctuations remains unclear. Further studies should assess what other variables (context, other cognitive processes, prestimulus cognitive state) might modulate these fluctuations. In particular, more ecological frameworks could be used (Freiwald et al., 2016), for instance using dynamic stimuli, to assess the extent to which the reported deflections depend on the stimulus features.

4.4 | Local–global framework

The local–global framework was used to test whether the activity of some recording sites was statistically coupled to the global fluctuations observed across sites. In particular, we found that the effect highly correlated with the local activity of brain areas involved in visual information processing, providing evidence that the global measures might be a novel signature of functional brain activity segregation taking place when a stimulus is processed in a task context. In addition, in the response-locked setting, the increase in mFC was significantly coupled to the local activity of brain areas in the motor cortex.

Here, we propose a first study to quantitatively asses local–global statistical relationships in a task-related context. Here, we do not aim to capture causal effects, but only time-concurrent local–global phenomena that may plausibly reflect a common functional network. This

study should pave the way for more sophisticated methods that can assess the role of each node when considering the whole network together. generalized linear models (GLMs), for instance, could serve this purpose. However, a difficulty in pursuing this approach lies in having insufficient statistical power, specially in short trials with a large number of recording sites. In addition, latent nonobserved variables should be considered to control for key hubs in the network that are not monitored but might coordinate global fluctuations. As previously mentioned, such improved models should take into account the modulation of the local–global coupling by other contextual variables or previous cognitive states. Further studies should also investigate directionality to assess direct influences of local activity on global fluctuations and vice versa, for instance by identifying particular global brain states that trigger local activity at certain nodes. This could be done by means of directionality measures such as Granger causality or directed information (Tauste Campo, 2020).

Another issue to take into consideration is the different time scales of local and global fluctuations. Physiologically meaningful local events such as HFOs or neuronal encoding can occur on the order of milliseconds (Arnulfo et al., 2015; Romo et al., 2002). At the same time, some studies have found global fluctuations with characteristic timescales of tens of seconds. In particular, resting state networks (RSN) below 0.1 Hz have been identified under the resting state condition both with fMRI and with time-resolved MEG (Brookes et al., 2011; Buckner et al., 2013; De Pasquale et al., 2010; Hipp et al., 2012). Other studies based on computational modeling or statistical inference have found global network states with a lifetime of around 200 ms (Buckner et al., 2013; Deco et al., 2019). This growing evidence suggests that different brain phenomena can be characterized by diverse spatial scales and evolve over the course of different temporal scales (Northoff et al., 2020; Vila-Vidal et al., 2020). Experimental designs and models linking activity at different spatial scales will have to face this phenomenon. Long resting-state iEEG recordings, for instance, could be used to test this hypothesis based on local intrinsic fast activations linked to slower-changing global states.

4.5 | Study limitations

The two main limitations of this study are the low number of patients and the limited spatial sampling inherent to the SEEG technique. Although this study has a methodological nature, some of the results reported here should be validated with a larger number of subjects, given the large intersubject variability of intracranial signals. In particular, patients should be chosen carefully according to their implantation schemes to better cover the visual-motor pathway in the aim to refine and better understand the bidirectional coupling between local activity and global fluctuations during this type of task.

In addition, our framework has been used to correlate fluctuations in global and local variables estimated by leveraging both on time and trials simultaneously as done in previous studies (PLV; Arnulfo et al., 2015; FC; Cruzat et al., 2018). The main advantage of this procedure is that it provides robust estimates when the number of trials is low, but inter- and intratrial variabilities become intermingled and are impossible to separate. Although out of the scope of this study, our framework could be adapted to regress the variability of global variables across trials at each time point using the local variables. This could be achieved by using single-trial estimates. However, time autocorrelation in low frequencies supposes a major drawback in pursuing this approach, specially in short trials where slow fluctuations cannot be captured. All in all, further studies should be designed with a larger number of trials to have sufficient statistical power to independently quantify inter- and intratrial variabilities.

CONFLICT OF INTEREST
The authors declare no conflicts of interest.

DATA AVAILABILITY STATEMENT
Due to institutional restrictions, the data that supports the findings of this study can be accessed only with a data sharing agreement.

PATIENT CONSENT STATEMENT

Informed consent was explicitly obtained from all participants prior to the recordings and the performance of the tasks.

ORCID

Manel Vila-Vidal 🔘 https://orcid.org/0000-0002-3280-2927
Adrià Tauste Campo 🔘 https://orcid.org/0000-0003-0982-4017

REFERENCES

Arnulfo, G., Hirvonen, J., Nobili, L., Palva, S., & Palva, J. M. (2015). Phase and amplitude correlations in resting-state activity in human stereotactical EEG recordings. *NeuroImage*, *112*, 114–127.

Axmacher, N., Schmitz, D. P., Wagner, T., Elger, C. E., & Fell, J. (2008). Interactions between medial temporal lobe, prefrontal cortex, and inferior temporal regions during visual working memory: A combined intracranial EEG and functional magnetic resonance imaging study. *Journal of Neuroscience*, *28*(29), 7304–7312.

Bassett, D. S., Wymbs, N. F., Porter, M. A., Mucha, P. J., Carlson, J. M., & Grafton, S. T. (2011). Dynamic reconfiguration of human brain networks during learning. *Proceedings of the National Academy of Sciences of the United States of America*, *108*(18), 7641–7646.

Bernstein, M., & Yovel, G. (2015). Two neural pathways of face processing: A critical evaluation of current models. *Neuroscience and Biobehavioral Reviews*, *55*, 536–546.

Bressler, S. L., & Menon, V. (2010). Large-scale brain networks in cognition: Emerging methods and principles. *Trends in Cognitive Sciences*, *14*(6), 277–290.

Brookes, M. J., Woolrich, M., Luckhoo, H., Price, D., Hale, J. R., Stephenson, M. C., Barnes, G. R., Smith, S. M., & Morris, P. G. (2011). Investigating the electrophysiological basis of resting state networks using magnetoencephalography. *Proceedings of the National Academy of Sciences of the United States of America*, *108*(40), 16783–16788.

Brunel, N., & Wang, X. J. (2001). Effects of neuromodulation in a cortical network model of object working memory dominated by recurrent inhibition. *Journal of Computational Neuroscience*, *11*(1), 63–85.

Buckner, R. L., Krienen, F. M., & Yeo, B. T. (2013). Opportunities and limitations of intrinsic functional connectivity MRI. *Nature Neuroscience*, *16*(7), 832–837.

Buzsáki, G., Anastassiou, C. A., & Koch, C. (2012). The origin of extracellular fields and currents-EEG, ECoG, LFP and spikes. *Nature Reviews Neuroscience*, *13*(6), 407–420.

Buzsáki, G., & Draguhn, A. (2004). Neuronal olscillations in cortical networks. *Science*, *304*(5679), 1926–1929.

Cardinale, F., Cossu, M., Castana, L., Casaceli, G., Schiariti, M. P., Miserocchi, A., Fuschillo, D., Moscato, A., Caborni, C., Arnulfo, G., & Lo Russo, G. (2013). Stereoelectroencephalography: Surgical methodology, safety, and stereotactic application accuracy in 500 procedures. *Neurosurgery*, *72*(3), 353–366.

Cruzat, J., Deco, G., Tauste-Campo, A., Principe, A., Costa, A., Kringelbach, M. L., & Rocamora, R. (2018). The dynamics of human cognition: Increasing global integration coupled with decreasing segregation found using iEEG. *NeuroImage*, *172*, 492–505.

De Pasquale, F., Della Penna, S., Snyder, A. Z., Lewis, C., Mantini, D., Marzetti, L., Belardinelli, P., Ciancetta, L., Pizzella, V., Romani, G. L., & Corbetta, M. (2010). Temporal dynamics of spontaneous MEG activity in brain networks. *Proceedings of the National Academy of Sciences of the United States of America*, *107*(13), 6040–6045.

Deco, G., Cruzat, J., & Kringelbach, M. L. (2019). Brain songs framework used for discovering the relevant timescale of the human brain. *Nature Communications*, *10*(1), 1–13.

Deco, G., & Rolls, E. T. (2005). Attention, short-term memory, and action selection: A unifying theory. *Progress in Neurobiology*, *76*(4), 236–256.

Deco, G., Tononi, G., Boly, M., & Kringelbach, M. L. (2015). Rethinking segregation and integration: Contributions of whole-brain modelling. *Nature Reviews Neuroscience*, *16*(7), 430–439.

Desikan, R. S., Ségonne, F., Fischl, B., Quinn, B. T., Dickerson, B. C., Blacker, D., Buckner, R. L., Dale, A. M., Maguire, R. P., Hyman, B. T., Albert, M. S., & Killiany, R. J. (2006). An automated labeling system for subdividing the human cerebral cortex on MRI scans into gyral based regions of interest. *NeuroImage*, *31*(3), 968–980.

Dobs, K., Isik, L., Pantazis, D., & Kanwisher, N. (2019). How face perception unfolds over time. *Nature Communications*, *10*(1), 1–10.

Engel, A. K., Moll, C. K., Fried, I., & Ojemann, G. A. (2005). Invasive recordings from the human brain: Clinical insights and beyond. *Nature Reviews Neuroscience*, *6*(1), 35–47.

Freiwald, W., Duchaine, B., & Yovel, G. (2016). Face processing systems: From neurons to real-world social perception. *Annual Review of Neuroscience*, *39*, 325–346.

Graf, A. B., Kohn, A., Jazayeri, M., & Movshon, J. A. (2011). Decoding the activity of neuronal populations in macaque primary visual cortex. In *Nature Neuroscience* (Vol. 14, pp. 239–247). Nature Publishing Group.

Grill-Spector, K., Weiner, K. S., Kay, K., & Gomez, J. (2017). The functional neuroanatomy of human face perception. *Annual Review of Vision Science*, *3*, 167–196.

Hipp, J. F., Hawellek, D. J., Corbetta, M., Siegel, M., & Engel, A. K. (2012). Large-scale cortical correlation structure of spontaneous oscillatory activity. *Nature Neuroscience*, *15*(6), 884–890.

Hubel, D. H., & Wiesel, T. N. (1959). Receptive fields of single neurones in the cat's striate cortex. *The Journal of Physiology*, *148*(3), 574–591.

Jonas, J., Jacques, C., Liu-Shuang, J., Brissart, H., Colnat-Coulbois, S., Maillard, L., & Rossion, B. (2016). A face-selective ventral occipito-temporal map of the human brain with intracerebral potentials. *Proceedings of the National Academy of Sciences of the United States of America*, *113*(28), E4088–E4097.

Kahana, M. J. (2006). The cognitive correlates of human brain oscillations. *Journal of Neuroscience*, *26*(6), 1669–1672.

Kahane, P., Minotti, L., Hoffmann, D., Lachaux, J.-P., & Ryvlin, P. (2003). Invasive EEG in the definition of the seizure onset zone: Depth electrodes. *Handbook of Clinical Neurophysiology*, *3*, 109–133.

Kohn, A., & Smith, M. A. (2005). Stimulus dependence of neuronal correlation in primary visual cortex of the macaque. *Journal of Neuroscience*, *25*(14), 3661–3673.

Lachaux, J.-P., Axmacher, N., Mormann, F., Halgren, E., & Crone, N. E. (2012). High-frequency neural activity and human cognition: Past, present and possible future of intracranial EEG research. *Progress in Neurobiology*, *98*(3), 279–301.

Lachaux, J. P., Rodriguez, E., Martinerie, J., & Varela, F. J. (1999). Measuring phase synchrony in brain signals. *Human Brain Mapping*, *8*(4), 194–208.

Lachaux, J. P., Rudrauf, D., & Kahane, P. (2003). Intracranial EEG and human brain mapping. In *Journal of Physiology* (Vol. 97, pp. 613–628). Elsevier.

Landi, S. M., & Freiwald, W. A. (2017). Two areas for familiar face recognition in the primate brain. *Science*, *357*(6351), 591–595.

Luna, R., Hernández, A., Brody, C. D., & Romo, R. (2005). Neural codes for perceptual discrimination in primary somatosensory cortex. *Nature Neuroscience*, *8*(9), 1210–1219.

Mitra, P. P., & Pesaran, B. (1999). Analysis of dynamic brain imaging data. *Biophysical Journal*, *76*(2), 691–708.

Munari, C., & Bancaud, J. (1985). The role of stereo-electroencephalography (SEEG) in the evaluation of partial epileptic seizures. In R. J. Porter & P. Morselli (Eds.), *The epilepsies* (pp. 267–306). Butterworths.

Narizzano, M., Arnulfo, G., Ricci, S., Toselli, B., Tisdall, M., Canessa, A., Fato, M. M., & Cardinale, F. (2017). SEEG assistant: A 3D Slicer extension to support epilepsy surgery. *BMC Bioinformatics*, *18*(1), 124.

Northoff, G., Wainio-Theberge, S., & Evers, K. (2020). Is temporo-spatial dynamics the "common currency" of brain and mind? In quest of "spatiotemporal neuroscience". *Physics of Life Reviews*, *33*, 34–54.

Palva, S., Monto, S., & Palva, J. M. (2010). Graph properties of synchronized cortical networks during visual working memory maintenance. *NeuroImage*, *49*(4), 3257–3268.

Pesaran, B., Vinck, M., Einevoll, G. T., Sirota, A., Fries, P., Siegel, M., Truccolo, W., Schroeder, C. E., & Srinivasan, R. (2018). Investigating large-scale brain dynamics using field potential recordings: Analysis and interpretation. *Nature Neuroscience*, *21*(7), 903–919.

Rey, H. G., Ahmadi, M., & Quian Quiroga, R. (2015). Single trial analysis of field potentials in perception, learning and memory. *Current Opinion in Neurobiology*, *31*, 148–155.

Rey, H. G., Fried, I., & Quian Quiroga, R. (2014). Timing of single-neuron and local field potential responses in the human medial temporal lobe. *Current Biology*, *24*(3), 299–304.

Romo, R., Hernández, A., Zainos, A., Lemus, L., & Brody, C. D. (2002). Neuronal correlates of decision-making in secondary somatosensory cortex. *Nature Neuroscience*, *5*(11), 1217–1225.

Salinas, E., & Romo, R. (1998). Conversion of sensory signals into motor commands in primary motor cortex. *Journal of Neuroscience*, *18*(1), 499–511.

Slepian, D., & Pollak, H. O. (1961). Prolate spheroidal wave functions, Fourier analysis and uncertainty—I. *Bell System Technical Journal*, *40*(1), 43–63.

Smith, M. A., & Kohn, A. (2008). Spatial and temporal scales of neuronal correlation in primary visual cortex. *Journal of Neuroscience*, *28*(48), 12591–12603.

Sporns, O., Tononi, G., & Kötter, R. (2005). The human connectome: A structural description of the human brain. *PLoS Computational Biology*, *1*(4), 245–251.

Tauste Campo, A. (2020). Inferring neural information flow from spiking data. *Computational and Structural Biotechnology Journal*, *18*, 2699–2708.

Tauste Campo, A., Principe, A., Ley, M., Rocamora, R., & Deco, G. (2018). Degenerate time-dependent network dynamics anticipate seizures in human epileptic brain. *PLoS Biology*, *16*(4), e2002580.

Tauste Campo, A., Martinez-Garcia, M., Nácher, V., Luna, R., Romo, R., & Deco, G. (2015). Task-driven intra- and interarea communications in primate cerebral cortex. *Proceedings of the National Academy of Sciences of the United States of America*, *112*(15), 4761–4766.

Thomson, D. J. (1982). Spectrum estimation and harmonic analysis. *Proceedings of the IEEE*, *70*(9), 1055–1096.

Thura, D., & Cisek, P. (2014). Deliberation and commitment in the premotor and primary motor cortex during dynamic decision making. *Neuron*, *81*(6), 1401–1416.

Van Vugt, B., Dagnino, B., Vartak, D., Safaai, H., Panzeri, S., Dehaene, S., & Roelfsema, P. R. (2018). The threshold for conscious report: Signal loss and response bias in visual and frontal cortex. *Science*, *360*(6388), 537–542.

Vila-Vidal, M., Capouskova, K., Atasoy, S., Kringelbach, M. L., & Deco, G. (2020). Uncovering the spatiotemporal scales of common neuromental constructs: Comment on "Is temporo-spatial dynamics the 'common currency' of brain and mind? In quest of 'spatiotemporal neuroscience'" by Georg Northoff et al. *Physics of Life Reviews*, *33*, 64–66.

Wang, N., Zhang, L., & Liu, G. (2015). EEG-based research on brain functional networks in cognition. *Bio-medical Materials and Engineering*, *26*(s1), S1107–S1114.

Wang, X., Zhen, Z., Song, Y., Huang, L., Kong, X., & Liu, J. (2016). The hierarchical structure of the face network revealed by its functional connectivity pattern. *Journal of Neuroscience*, *36*(3), 890–900.

Wang, X. J. (2002). Probabilistic decision making by slow reverberation in cortical circuits. *Neuron*, *36*(5), 955–968.

Zaveri, H. P., Duckrow, R. B., & Spencer, S. S. (2006). On the use of bipolar montages for time-series analysis of intracranial electroencephalograms. *Clinical Neurophysiology*, *117*, 2102–2108.

Zhen, Z., Fang, H., & Liu, J. (2013). The hierarchical brain network for face recognition. *PLoS One*, *8*(3), 59886.

SUPPORTING INFORMATION

Additional supporting information can be found online in the Supporting Information section at the end of this article.

How to cite this article: Vila-Vidal, M., Khawaja, M., Carreño, M., Roldán, P., Rumià, J., Donaire, A., Deco, G., & Tauste Campo, A. (2022). Assessing the coupling between local neural activity and global connectivity fluctuations: Application to human intracranial electroencephalography during a cognitive task. *Human Brain Mapping*, 1–20. https://doi.org/10.1002/hbm.26150